

Molecular dynamics study on the effect of cooling rate on the mechanical behavior of B2-CuZr enhanced bulk-metallic glass composites

Huahuai Shen(沈华淮), Kai Wang(王楷), Chenghao Chen(陈城豪), Jiaqing Wu(伍嘉卿), Mixun Zhu(朱谧询), Hongtao Zhong(钟泓涛), Yuanzheng Yang(杨元政), and Xiaoling Fu(付小玲)
Citation: Chin. Phys. B, 2025, 34 (**12**): 128102. DOI: 10.1088/1674-1056/adf9fa
http://cpb.iphy.ac.cn; http://iopscience.iop.org/cpb

What follows is a list of articles you may be interested in

Plastic deformation mechanism of *γ*-phase U-Mo alloy studied by molecular dynamics simulations

Chang Wang(王畅), Peng Peng(彭芃), and Wen-Sheng Lai(赖文生)
Chin. Phys. B, 2025, 34 (**1**): 018101. DOI: 10.1088/1674-1056/ad925e

Unravelling biotoxicity of graphdiyne: Molecular dynamics simulation of the interaction between villin headpiece protein and graphdiyne

Bei-Wei Zhang(张贝薇), Bing-Quan Zhang(张兵权), Zhi-Gang Shao(邵志刚), and Xianqiu Wu(吴先球)
Chin. Phys. B, 2024, 33 (**11**): 118102. DOI: 10.1088/1674-1056/ad7af5

Amorphous transformation of ternary $Cu_{45}Zr_{45}Ag_{10}$ alloy under microgravity condition

Ming-Hua Su(苏明华), Fu-Ping Dai(代富平), and Ying Ruan(阮莹)
Chin. Phys. B, 2022, 31 (**9**): 098106. DOI: 10.1088/1674-1056/ac67c9

Modeling of microporosity formation and hydrogen concentration evolution during solidification of an Al-Si alloy

Qingyu Zhang(张庆宇), Dongke Sun(孙东科), Shunhu Zhang(章顺虎), Hui Wang(王辉), Mingfang Zhu(朱鸣芳)
Chin. Phys. B, 2020, 29 (**7**): 078104. DOI: 10.1088/1674-1056/ab8abb

High quality sub-monolayer, monolayer, and bilayer graphene on Ru(0001)

Xu Wen-Yan (徐文焱), Huang Li (黄立), Que Yan-De (阙炎德), Li En (李恩), Zhang Hai-Gang (张海刚), Lin Xiao (林晓), Wang Ye-Liang (王业亮), Du Shi-Xuan (杜世萱), Gao Hong-Jun (高鸿钧)
Chin. Phys. B, 2014, 23 (**9**): 098101. DOI: 10.1088/1674-1056/23/9/098101

Molecular dynamics study on the effect of cooling rate on the mechanical behavior of B2-CuZr enhanced bulk-metallic glass composites

Huahuai Shen(沈华淮), Kai Wang(王楷), Chenghao Chen(陈城豪), Jiaqing Wu(伍嘉卿), Mixun Zhu(朱谧询), Hongtao Zhong(钟泓涛), Yuanzheng Yang(杨元政), and Xiaoling Fu(付小玲)†

School of Materials and Energy, Guangdong University of Technology, Guangzhou 510006, *China*

(Received 3 May 2025; revised manuscript received 25 July 2025; accepted manuscript online 11 August 2025)

Metallic glasses (MG) have attracted considerable attention due to their high hardness, high fracture strength, and excellent corrosion resistance. However, their poor room-temperature plasticity limits their widespread application to some extent. To address this issue, researchers have attempted to introduce crystalline phases into MG to enhance their mechanical properties. Molecular dynamics (MD) simulations are a powerful tool for investigating the properties and deformation mechanisms of amorphous/crystalline dual-phase composite materials. In this study, MD simulations were employed to explore the effect of different cooling rates on the tensile properties of B2-CuZr enhanced bulk-metallic glass composites (BMGCs). Molecular dynamics simulations were conducted on B2-CuZr enhanced BMGCs at an ambient temperature of 300 K. The results indicate that as the cooling rate decreases, from 100 K/ps, 10 K/ps, 1 K/ps, 0.5 K/ps, the content of $\langle 0,0,12,0\rangle$ polyhedra increases, resulting in improved mechanical strength but reduced plasticity. In this study, as the cooling rate increases from 0.5 K/ps to 100 K/ps, the deformation strain increases from $\varepsilon = 0.407$ to $\varepsilon = 0.466$. However, the specimens with a cooling rate of 1 K/ps display notably better plasticity, deviating from the trend. This enhancement in plasticity is attributed to the increased presence of $\langle 0,2,8,5\rangle$ polyhedra in the 1 K/ps sample. The findings of this study provide valuable insights for the design and fabrication of high-performance metallic glass materials.

Keywords: metallic glass matrix composite, cooling rate, molecular dynamics, icosahedron

PACS: 81.05.Pj, 64.70.pe, 61.20.Ja, 81.40.Lm

DOI: 10.1088/1674-1056/adf9fa **CSTR:** 32038.14.CPB.adf9fa

1. Introduction

Metallic glass, also known as amorphous alloy, is a solid material formed when a metal undergoes rapid cooling and solidifies without crystallization.[1] Due to the lack of long-range periodicity and translational symmetry in the atomic arrangement within metallic glass compared to conventional crystalline materials in three-dimensional space,[2] its structure is free from defects such as dislocations and grain boundaries. This unique structure endows metallic glass with many remarkable properties, including high strength and hardness, high elastic strain limit, excellent wear resistance, superior corrosion resistance, and outstanding castability.[3] These exceptional properties have attracted significant attention from researchers both domestically and internationally.[3–7] During the deformation process of amorphous materials, shear transformation zones (STZs) undergo localized atomic rearrangements, resulting in the formation of a shear band, which plays a critical role in plastic deformation at room temperature.[8,9] Despite their outstanding properties, metallic glasses exhibit limited plasticity due to the highly localized shear banding during tensile deformation at room temperature, which rapidly propagates and leads to catastrophic brittle fracture. This severely restricts their applications in many practical engineering fields.[10–14]

Currently, extensive research has demonstrated that the introduction of crystalline particles or secondary phase into amorphous matrices can effectively hinder shear band propagation and promote the nucleation of STZs at interfaces, leading to the formation of multiple shear bands and thereby enhancing the plasticity of metallic glasses.[15–21] Among these approaches, incorporating secondary phase has proven to be particularly effective, resulting in the development of metallic glass matrix composites.[12,22,23] The introduction of secondary phase into the amorphous matrix not only enhances the deformation capability of metallic glasses at room temperature but also suppresses shear band propagation, allowing shear bands to accommodate more plastic deformation. When shape memory alloys are incorporated as the second phase into the amorphous matrix, they form crystalline/amorphous composites with excellent plasticity and work-hardening capability.[24–28] This is attributed to the strain-induced martensitic transformation (MT) and the "blocking" effect exerted by the microscaled B2-CuZr crystals on the shear bands.[29–31]

As is well known, the cooling rate is one of the critical factors in the formation of metallic glass.[32,33] The properties of metallic glass are determined by its internal atomic

†Corresponding author. E-mail: fuxiaoling@gdut.edu.cn

© 2025 Chinese Physical Society and IOP Publishing Ltd. All rights, including for text and data mining, AI training, and similar technologies, are reserved.

configuration, and the atomic structure of metallic glass can be regarded as the solidified form of frozen liquid. However, different cooling rates influence the arrangement of atoms within the metallic glass, thereby affecting its structural characteristics.[34,35] Consequently, the properties of metallic glass can be tuned by altering the cooling rate. Many studies have been conducted on the influence of cooling rate on the properties of metallic glass, and it has been shown that metallic glass exhibits higher strength at lower cooling rates.[32,36,37] Metallic glasses generated under high cooling rates tend to form structures with increased disorder and higher-energy states. These high-energy states are beneficial for enhancing the plasticity of metallic glasses.[38] Moreover, the short-range ordered structures based on tetrahedral models, particularly the icosahedral-like polyhedral configurations, are considered essential components of metallic glasses. Among them, the full icosahedron (Voronoi index $\langle 0,0,12,0\rangle$, FI) and the distorted icosahedron $\langle 0,2,8,2\rangle$ play a significant role in influencing the structural and mechanical properties of metallic glasses.[39–42] Studies have shown that the high-density packing of full icosahedra is closely associated with the high strength of metallic glasses and is considered the most stable structure.[43] This is because the fivefold symmetry of the FI structure exhibits a high coordination number and dense atomic packing, effectively hindering atomic slip and dislocation motion, thereby enhancing the material's strength.[40] For example, Cheng *et al.*[40] found in their study on Cu–Zr metallic glasses that as the fraction of FI structures increases, the yield strength of the material significantly improves, while the plastic strain gradually decreases. The high stability of the FI structure leads to a reduced capacity for plastic deformation in metallic glasses. This is because the high symmetry and dense packing of FI make it more difficult for local regions to initiate and propagate shear bands.[41]

In this study, the evolution of shear bands, Voronoi polyhedra, and crystalline structures in B2-CuZr enhanced bulk-metallic glass composites (BMGCs) under tensile deformation was investigated at four different cooling rates (0.5 K/ps, 1 K/ps, 10 K/ps, 100 K/ps). The study reveals the effects of atomic-scale interactions — including martensitic transformation, localized shear softening, and strain concentration at crystalline-amorphous interfaces — on the structural and mechanical properties of BMGCs. Note that the cooling rate employed in the current molecular dynamics study is much higher than those in the experiments limited by the computational cost. This research is more qualitative, aiming to investigate the underlying mechanisms of the effect of the cooling rate on the mechanical performance of B2-CuZr enhanced BMGCs.

2. Methodology

In this study, molecular dynamics (MD) simulations[44] were performed using the open-source software Large-scale Atomic/Molecular Massively Parallel Simulator (LAMMPS)[45] to investigate the tensile behavior of B2-CuZr enhanced BMGCs under different cooling rates. The atomic interactions in the B2-CuZr enhanced BMGCs were described using the embedded atom method (EAM) potential developed by Mendelev *et al.*[46] This potential effectively captures the martensitic transformation process in B2-CuZr crystals and has been successfully applied in simulations of B2-CuZr metallic glass composites.[47,48] For samples embedded with brick-shaped B2-CuZr precipitates, it is easier to observe phase transformation behavior due to high strain concentration caused by the high curvature of the sharp corners.[49,50]

First, a $Cu_{50}Zr_{50}$ amorphous thin slab with dimensions of 31.4 nm (X) × 15.7 nm (Y) × 2.6 nm (Z), containing 73728 atoms, was prepared. Within this slab, nine block regions, each measuring 7.85 nm (X) × 1.64 nm (Y) × 2.6 nm (Z), were fixed. Fully periodic boundary conditions (PBCs) were imposed in all three directions during the whole simulation process. The integration time step is set as 0.001 ps. The remaining part of the slab, excluding these block regions, was equilibrated at a temperature of 2100 K under an external pressure of 0 GPa within an NPT ensemble (constant number of atoms, constant pressure and constant temperature) for 0.05 ns to ensure complete melting. Subsequently, the system was quenched to 300 K at cooling rates of 0.5 K/ps (1 K/ps, 10 K/ps, and 100 K/ps) under the NPT ensemble to achieve a glassy state. Finally, the entire sample was relaxed at 300 K for 0.2 ns to obtain a relaxed atomic configuration, thereby generating samples with different cooling rates. The Nosé–Hoover thermostat was employed to control the temperature and pressure in the isothermal-isobaric ensemble. Based on our previous calculation, the martensitic transformation temperature for B2-CuZr enhanced BMGCs with a similar composition roughly ranges from 137 K to 190 K.[51] To prevent the phase instability of B2 precipitate at cryogenic temperature, the processing temperature in this work is carefully chosen as 300 K. The model construction process is illustrated in Fig. 1. The volume fractions of the amorphous phase and the crystalline phase within these composites were 78%±3%, 22±3%, respectively.

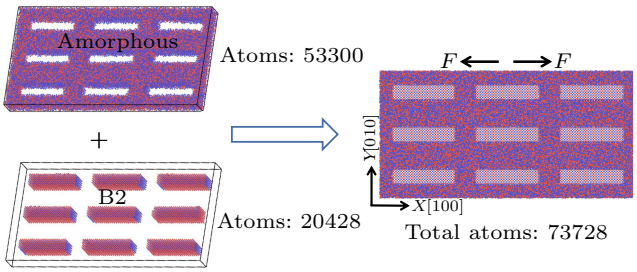


Fig. 1. Schematic of the modeling process for the B2-CuZr enhanced BMGCs.

Before loading, periodic boundary conditions were applied in the X, Y, and Z directions for the B2-CuZr enhanced

BMGCs sample. The sample was then subjected to uniaxial tensile simulation along the X-direction at a strain rate of 2×10^{10} s^{-1} at 300 K until the total tensile strain reached 80%. The pressure in the Y and Z directions was maintained at 0 GPa. To characterize the atomic inelastic deformation, the deformed atomic configuration was compared with the initial configuration, and shear deformation was quantified using the η_i^{Mises} parameter proposed by Shimizu *et al.*[52] A larger η_i^{Mises} value indicates a higher local shear strain experienced by the atom. Throughout the entire simulation, analyses were performed using the polyhedral template matching algorithm (PTM) and η_i^{Mises} parameter in the visualization software OVITO.[53] The measurement of shear band width was carried out by exporting images of the shear bands from OVITO, measuring the width of each shear band in the image, and then multiplying it by the ratio of the actual crystal length to the crystal length in the image to obtain the actual shear band width.

3. Results and analysis

3.1. Deformation process of B2-CuZr enhanced BMGCs under tension

Figure 2 presents a comparison of the stress–strain curves for B2-CuZr enhanced BMGCs under four different cooling rates (0.5 K/ps, 1 K/ps, 10 K/ps, 100 K/ps). As shown in Fig. 2, all samples exhibit a secondary yielding phenomenon during the tensile process. As the cooling rate increases, the yield strength gradually decreases, which is consistent with both experimental[36] and simulation[32,37] results. Among them, the sample with the slowest cooling rate of 0.5 K/ps exhibits the highest yield strength of 4.327 GPa (Table 1 and Fig. 3(a)). The characteristic points O_{I} (O_{II}, O_{III}, O_{IV}), A_{I} (A_{II}, A_{III}, A_{IV}), B_{I} (B_{II}, B_{III}, B_{IV}), C_{I} (C_{II}, C_{III}, C_{IV}), D_{I} (D_{II}, D_{III}, D_{IV}), E_{I} (E_{II}, E_{III}, E_{IV}), and F_{I} (F_{II}, F_{III}, F_{IV}) are used to describe the related microstructural evolution of the samples under uniaxial tensile strain. The snapshots of local shear strain and corresponding phase transformations of the crystalline phase at characteristic points for each model (0.5 K/ps, 1 K/ps, 10 K/ps, 100 K/ps) are listed in Fig. 5.

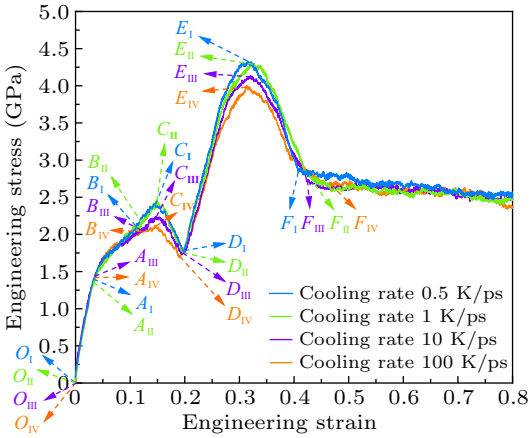


Fig. 2. Stress–strain curves of B2-CuZr enhanced BMGCs under four different cooling rates (0.5 K/ps, 1 K/ps, 10K/ps, 100 K/ps).

Table 1. The maximum yield strength (τ_y), steady-state stress (τ_s), shear band width (W), deformation strain (O–F), elastic deformation (O–A), and plastic deformation (A–F) of B2-CuZr enhanced BMGCs.

Cooling rate	$\tau_y(E)$	$\tau_s(F)$	W (Å)	Deformation strain (O–F)	Elastic strain (O–A)	Plastic strain (A–F)
0.5 K/ps	4.327	2.865	4 ∼ 13	0.407	0.033	0.374
1 K/ps	4.298	2.716	5 ∼ 15	0.440	0.033	0.407
10 K/ps	4.136	2.714	5 ∼ 16	0.424	0.035	0.389
100 K/ps	4.000	2.654	4 ∼ 16	0.466	0.035	0.431

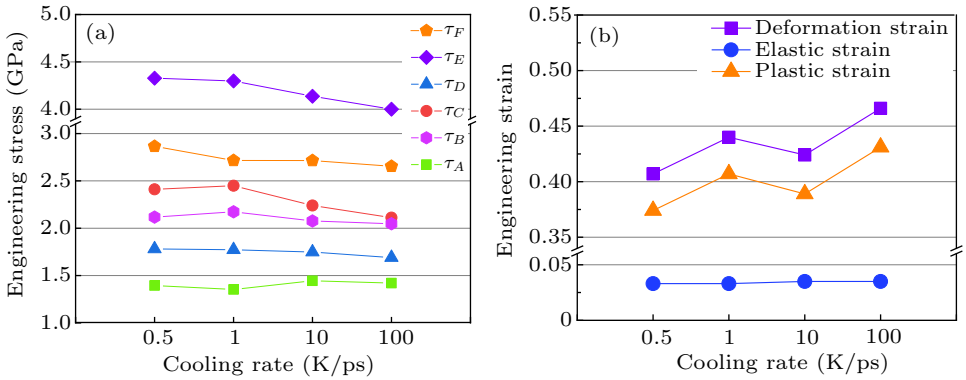


Fig. 3. The stress and strain variations of B2-CuZr enhanced BMGCs at different cooling rates (0.5 K/ps, 1 K/ps, 10 K/ps, 100 K/ps). (a) The stress corresponding to each characteristic point. (b) The variation of the elastic strain, plastic strain, and deformation strain.

Figures 4(a)–4(d) represent the stress–strain curves and corresponding potential energy evolution diagrams of B2-CuZr enhanced BMGCs samples under cooling rates of 0.5 K/ps, 1 K/ps, 10 K/ps, and 100 K/ps, respectively. Figure 5 presents snapshots and corresponding phase transformation diagrams of the samples at different strains under the four cool-

ing rates. As shown in Fig. 2, the stress–strain curves exhibit similar trends across the four different cooling rates. Therefore, the tensile process at a cooling rate of 0.5 K/ps is selected as a representative case for analysis. As observed in Figs. 4 and 5, during the O_I–A_I stage, which corresponds to the elastic deformation stage of the amorphous matrix and B2 crystalline phase (Fig. 5(a), O_I–A_I), the average potential energy of the sample increases with increasing strain (Fig. 4(a)). The first yield point is reached at the A_I point. In the A_I–B_I stage, the B2 phase undergoes yielding and transforms into the R phase (Fig. 5(a), A_I phase evolution), resulting in a decrease in the average potential energy (Fig. 4(a)). The B2 phase is completely transformed into the R phase at the B_I point (Fig. 5(a), B_I phase evolution). In the B_I–C_I stage, the R phase undergoes elastic deformation, leading to an increase in the average potential energy (Fig. 4(a)). The second yield point is reached at the C_I point. In the C_I–D_I stage, the R phase undergoes yielding and gradually transforms into the BCT phase (Fig. 5(a), C_I–D_I phase evolution). The appearance of the BCT phase causes a decrease in the average potential energy of the sample (Fig. 4(a)). At the D_I point, the R phase is completely transformed into the BCT phase (Fig. 5(a), D_I phase evolution). In the D_I–E_I stage, the BCT phase undergoes elastic deformation (Fig. 5(a), D_I–E_I phase evolution), leading to an increase in the average potential energy (Fig. 4(a)). In the E_I–F_I stage, the BCT phase gradually develops broken atoms (Fig. 5(a), E_I phase evolution), and at the F_I point, the broken atoms span the entire crystal (Fig. 5(a), F_I phase evolution). At the F_I point, atoms near the four corners and the central region of the crystal sample experience high strain (Fig. 5, F_I-shear strain and phase evolution). After the F_I point, the sample undergoes flow strain, indicating the failure of the entire sample.

The evolution of the atomic von Mises strain and the corresponding PTM is shown in Fig. 6. At the B_I point, a diffusive shear transformation zone (STZ) emerges within the amorphous matrix (Fig. 6(a), B_I). From point B_I to C_I, the shear strain in the amorphous matrix gradually increases (Fig. 6(a), B_I–C_I). However, at point C_I, a distinct banded region surrounding the crystalline particles appears (Fig. 6(a), C_I), indicating the shear strain region associated with the phase transformation from the B2 phase to the R phase, as well as the elastic deformation of the R phase. From point C_I to D_I, the local shear strain distribution within the amorphous matrix continues to rise, while the local strain in the banded region around the crystalline particles increases slightly, but remains lower than that in the amorphous region (Fig. 6(a), C_I–D_I). From point D_I to E_I, STZs nucleate at the four-corner regions of the brick-shaped crystalline and around the crystal/amorphous interfaces (Fig. 6(a), D_I–E_I). From point E_I to F_I, more and more STZs are activated and coalesce into shear bands (Fig. 6(a), E_I–F_I). When the shear bands are obstructed by brick-shaped crystalline, the central atoms of the blocks experience higher strain until the blocks split into two pieces from the central region. Consequently, the shear bands in the amorphous matrix penetrate through the crystalline particles and connect throughout the entire sample. The highly localized strain around the crystal/amorphous interfaces results in a fully developed shear band at point F_I. Beyond point F_I, the stress enters a steady-state flow regime, indicating the failure of the system.

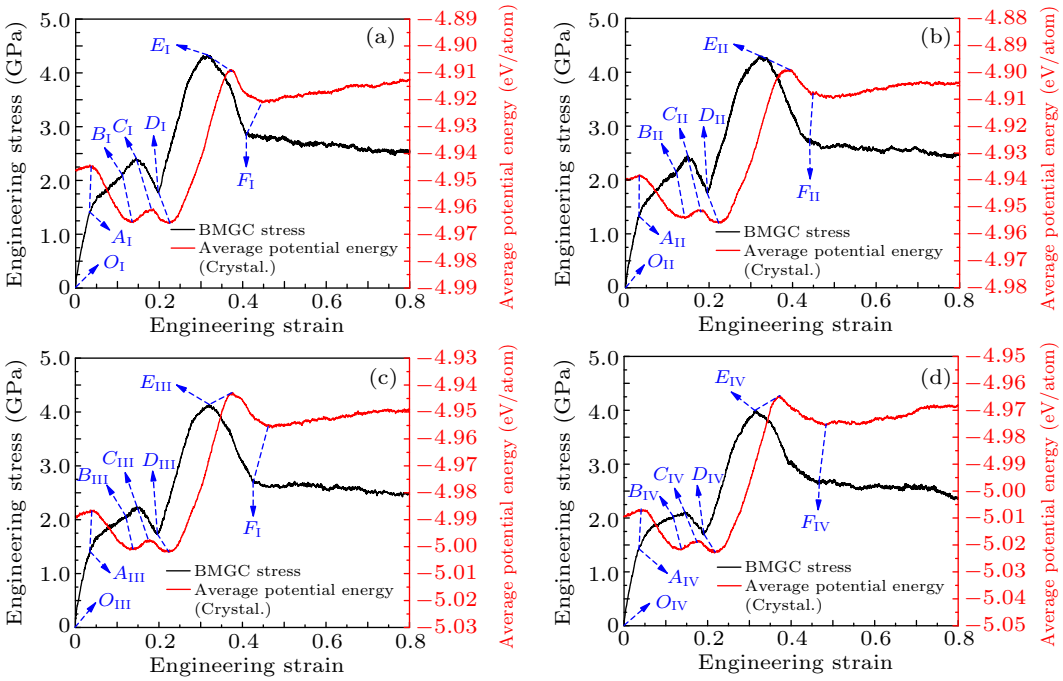


Fig. 4. Stress–strain curves and corresponding potential energy evolution of B2-CuZr enhanced BMGCs under different cooling rates: (a) 0.5 K/ps, (b) 1 K/ps, (c) 10 K/ps, (d) 100 K/ps.

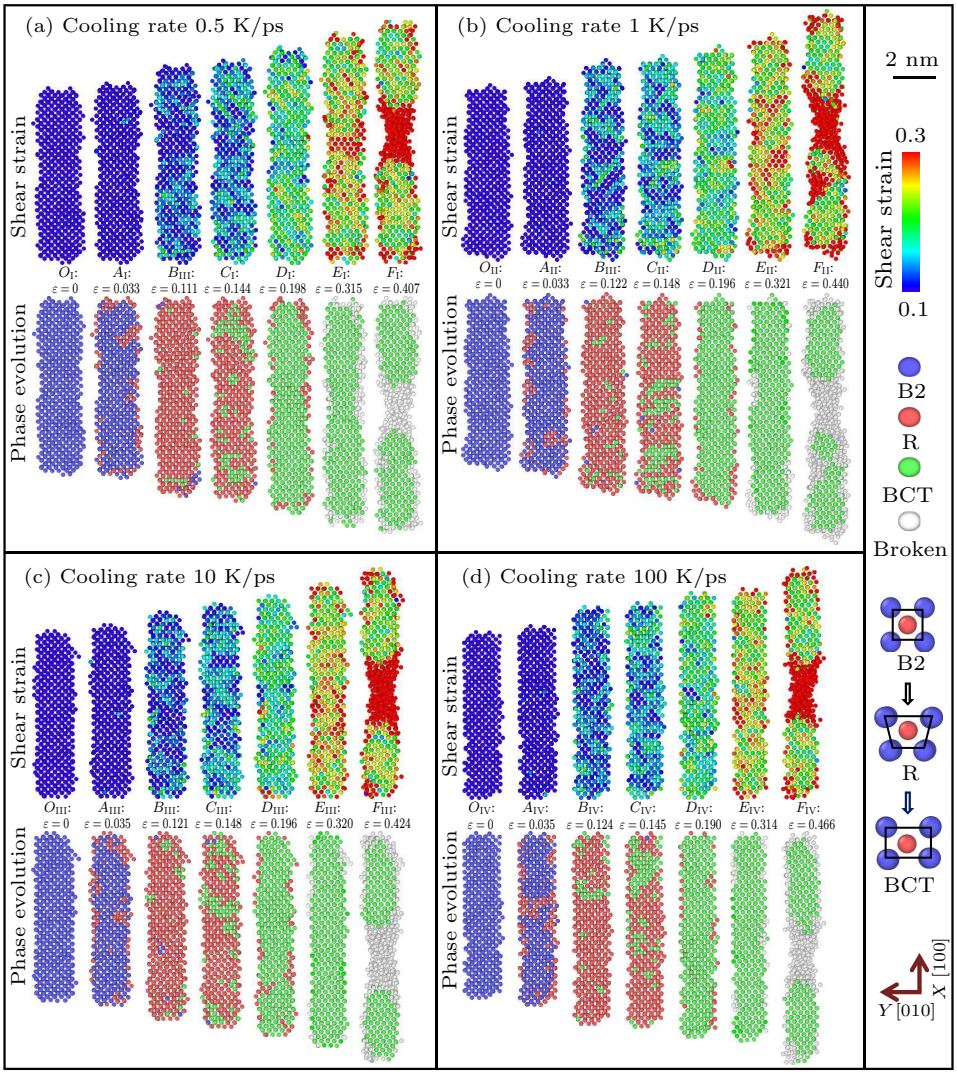


Fig. 5. Evolution of local shear strain distribution and the results of the PTM for the B2-CuZr enhanced BMGCs at different strains under various cooling rates: (a) 0.5 K/ps, (b) 1 K/ps, (c) 10 K/ps, (d) 100 K/ps.

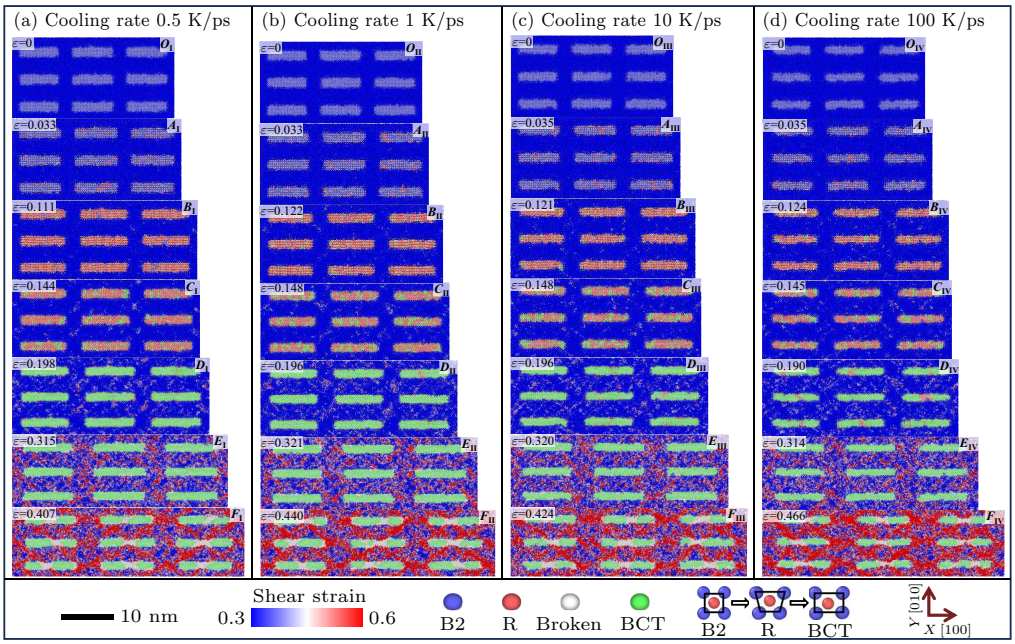


Fig. 6. Atomic shear strain evolution of the B2-CuZr enhanced BMGCs under different strain levels and cooling rates: (a) 0.5 K/ps, (b) 1 K/ps, (c) 10 K/ps, (d) 100 K/ps.

3.2. Analysis of Voronoi polyhedral clusters

Voronoi polyhedral cluster is defined as a polyhedron of the minimal volume that completely encloses a given atom, constructed by the perpendicular bisecting planes of the lines connecting the atom to its neighboring atoms. The Voronoi index $\langle n_3, n_4, n_5, n_6, \ldots, n_i \rangle$ is used to characterize the structures of various Voronoi polyhedral clusters, where n_i represents the number of polygons with i edges, with i typically ranging from 3 to 6.[41] Atomic clusters with Voronoi indices of $\langle 0,0,12,0 \rangle$ (FI) and $\langle 0,2,8,2 \rangle$ exhibit higher five-fold local symmetry (LFFS),[54] whereas atomic clusters with indices of $\langle 0,2,8,5 \rangle$ and $\langle 0,3,6,4 \rangle$ display lower five-fold local symmetry.

Figure 7 shows the effect of different cooling rates on the fraction of four Voronoi polyhedra in B2-CuZr enhanced BMGCs. With the decrease in cooling rate, the fraction of polyhedra with high fivefold local symmetry, $\langle 0,0,12,0 \rangle$, significantly increases. This trend is in strong agreement with the characterization results of FI (Fig. 8). The increase in FI leads to an enhancement in the strength of the sample.[40] It is noteworthy that polyhedra with similar symmetric characteristics, $\langle 0,2,8,2 \rangle$, also show an increasing trend. When combined with the stress–strain curve in Fig. 2, the increase in these two structurally stable polyhedra types is closely correlated with the enhancement of material strength, indicating that they play a key role in maintaining the mechanical strength of the material. Zhou *et al.*[48] indicates that an increase in shear band width contributes to enhanced plasticity of the material. In addition, the study by Pan *et al.*[55] revealed the presence of a softening zone within the shear band, with its width increasing from 40 μm to 160 μm as the plastic strain increased from 2% to 6%. Therefore, the widening of the shear band is generally associated with an enlarged softening region, which in turn contributes to enhanced plastic deformability of the material. In this study, as the cooling rate increases from 0.5 K/ps to 100 K/ps, the deformation strain increases from $\varepsilon = 0.407$ to $\varepsilon = 0.466$. This trend is generally consistent with the results shown in Table 1, where the shear band width increases with higher cooling rates, thereby enhancing the plastic deformation capability of the sample.

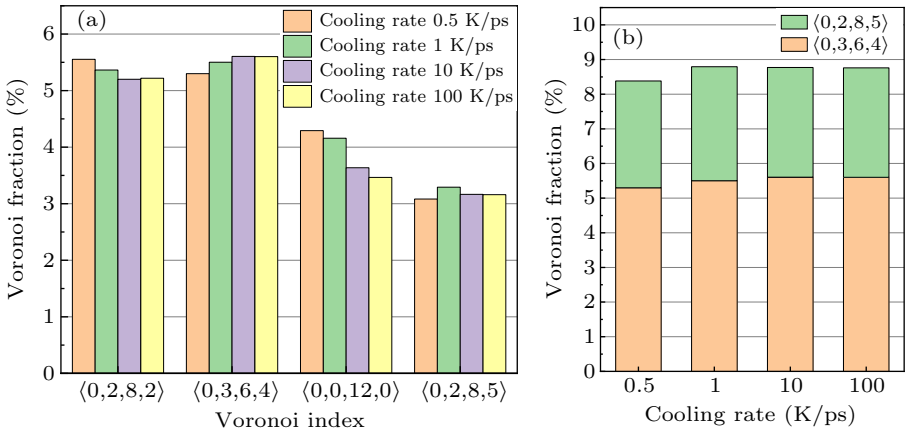


Fig. 7. Polyhedral analysis of the B2-CuZr enhanced BMGCs under cooling rates of 0.5 K/ps, 1 K/ps, 10 K/ps, and 100 K/ps. (a) Fractions of various Voronoi polyhedral. (b) The fraction of the combined $\langle 0,2,8,5 \rangle$ and $\langle 0,3,6,4 \rangle$ polyhedral.

However, the sample with a cooling rate of 1 K/ps ($\varepsilon = 0.440$) exhibits superior plasticity compared to the sample with a cooling rate of 10 K/ps ($\varepsilon = 0.424$) (Table 1 and Fig. 3(b)). The study by Amigo *et al.*[56] indicates that an increase in the coordination number of polyhedra can be regarded as a stress-relief mechanism within the system, ultimately leading to sample softening. Moreover, the work by Liu *et al.*[57] suggests that a reduction in stress helps suppress shear band propagation. Therefore, an increase in high-coordination-number polyhedra is beneficial for enhancing the plasticity of the material. As shown in Fig. 7(b), the sample cooled at 1 K/ps contains more high-coordination polyhedra than that cooled at 10 K/ps, resulting in better plasticity. Idury *et al.*[58] found that the larger bond energy of $\langle 0,2,8,5 \rangle$ clusters leads to this cluster's higher free volume. Due to the long-range elastic interactions between these free volume-rich clusters, they self-organize to form shear bands. Therefore, the increase in the $\langle 0,2,8,5 \rangle$ cluster content results in the formation of more shear bands, thereby enhancing plasticity. Atomic clusters with lower LFFS values contain more free volume.[59] Therefore, the $\langle 0,2,8,5 \rangle$ and $\langle 0,3,6,4 \rangle$ polyhedra are favorable for plastic deformation. Feng *et al.*[60] found that the lower degree of fivefold local symmetry in $\langle 0,2,8,5 \rangle$ clusters leads to an increased defect density, making them more susceptible to plastic deformation compared to the complete icosahedral clusters $\langle 0,0,12,0 \rangle$. The underlying reason for the superior plasticity observed in the 100 K/ps sample can be analyzed as follows: although the content of $\langle 0,2,8,5 \rangle$ clusters is comparable to that in the 10 K/ps sample, the fraction of full icosahedral (FI) structures is significantly lower. Given that FI structures play a crucial role in hindering shear band propagation and constraining plastic deformation, a reduced FI frac-

tion is generally associated with enhanced plasticity. Moreover, the FI content in the 100 K/ps sample is substantially lower than that in the 1 K/ps sample. This microstructural characteristic provides a reasonable explanation for the superior plastic deformation capability exhibited by the 100 K/ps sample.

From Fig. 7(a), it can be observed that the sample with a cooling rate of 1 K/ps has a higher content of $\langle 0,2,8,5\rangle$ clusters compared to the sample with a cooling rate of 10 K/ps, which in turn leads to an enhancement in the plasticity of the former sample. In conclusion, we believe that the increase in $\langle 0,2,8,5\rangle$ clusters is responsible for the improved plastic deformation in the sample with a cooling rate of 1 K/ps.

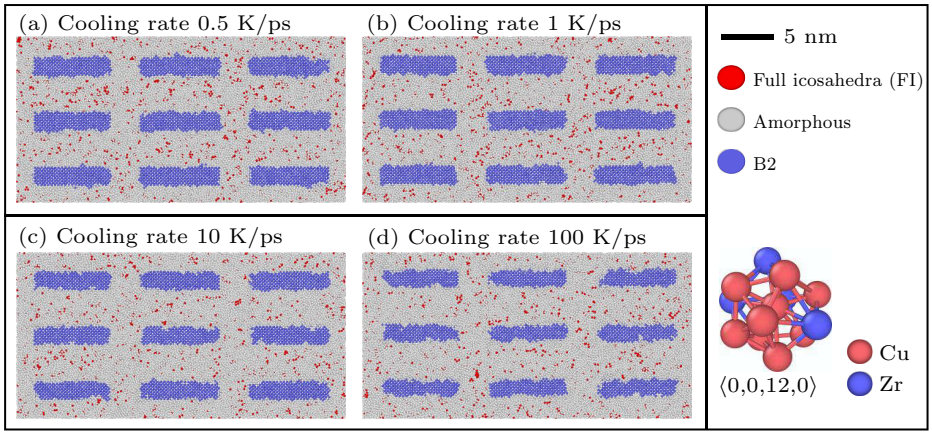


Fig. 8. FI characterization of B2-CuZr enhanced BMGCs under different cooling rates: (a) 0.5 K/ps, (b) 1 K/ps, (c) 10 K/ps, (d) 100 K/ps.

4. Conclusion

In this study, molecular dynamics simulations were employed to investigate the effect of cooling rate on the tensile behavior of B2-CuZr enhanced BMGCs. As the cooling rate decreases, the fraction of full icosahedra (FI) increases, leading to enhanced sample strength but reduced plasticity. In this study, as the cooling rate increases from 0.5 K/ps to 100 K/ps, the deformation strain increases from $\varepsilon = 0.407$ to $\varepsilon = 0.466$. However, the specimen cooled at 1 K/ps exhibits a higher fraction of $\langle 0,2,8,5\rangle$ polyhedra compared to that cooled at 10 K/ps, resulting in enhanced plastic deformation capability. Therefore, by controlling the cooling rate, the content of polyhedra can be adjusted, enabling the development of B2-CuZr enhanced BMGCs with desired properties.

Acknowledgements

The work was supported by the National Natural Science Foundation of China (Grant No. 52471005) and the Guangdong Basic and Applied Basic Research Foundation (Grant No. 2024A1515010878).

References

[1] Sohrabi S, Fu J, Li L, Zhang Y, Li X, Sun F, Ma J and Wang W H 2024 *Progress in Materials Science* **144** 101283
[2] Lou H, Zeng Z, Zhang F, Chen S, Luo P, Chen X, Ren Y, Prakapenka V B, Prescher C, Zuo X, Li T, Wen J, Wang W H, Sheng H and Zeng Q 2020 *Nat. Commun.* **11** 314
[3] Sayad S, Khanzadeh M, Alahyarizadeh G and Amigo N 2023 *Sci. Rep.* **13** 16109
[4] Wang P, Wang J Q, Li H, Yang H, Huo J, Wang J, Chang C, Wang X, Li R W and Wang G 2017 *J. Alloys Compd.* **701** 759
[5] Yue X, Brechtl J, Wang F, Chang Z, Liaw P K and Fan C 2020 *Materials & Design* **191** 108660
[6] Gludovatz B, Granata D, Thurston K V S, Löffler J F and Ritchie R O 2017 *Acta Materialia* **126** 494
[7] Liang S X, Sun L, Loza K, Zerebecki S, Jia Z, Yang Y, Qiao J, Zhang L C and Reichenberger S 2025 *Applied Surface Science* **679** 161269
[8] Tao K, Li F, Liu Y, Pineda E, Song K and Qiao J 2024 *International Journal of Plasticity* **174** 103873
[9] Wang N, Ding J, Yan F, Asta M, Ritchie R O and Li L 2018 *npj Computational Materials* **4** 19
[10] Chen W, Zhou H, Liu Z, Ketkaew J, Shao L, Li N, Gong P, Samela W, Gao H and Schroers J 2018 *Acta Materialia* **145** 477
[11] Dong Q, Tan J, Li C, Sarac B and Eckert J 2024 *Composites Part B: Engineering* **280** 111453
[12] Wang W H 2012 *Progress in Materials Science* **57** 487
[13] Hofmann D C 2010 *Science* **329** 1294
[14] Li D M, Chen L S, Yu P, Ding D and Xia L 2020 *Chin. Phys. Lett.* **37** 086401
[15] Song K, Pauly S, Zhang Y, Li R, Gorantla S, Narayanan N, Kühn U, Gemming T and Eckert J 2012 *Acta Materialia* **60** 6000
[16] Pauly S, Liu G, Wang G, Kühn U, Mattern N and Eckert J 2009 *Acta Materialia* **57** 5445
[17] Li J, Chen X and Huang F 2018 *J. Alloys Compd.* **737** 271
[18] Tong X, Wang G, Yi J, Ren J, Pauly S, Gao Y, Zhai Q J, Mattern N, Dahmen K A and Liaw P K 2016 *International Journal of Plasticity* **77** 141
[19] Sterwerf C, Kaub T, Deng C, Thompson G B and Li L 2017 *Thin Solid Films* **626** 184
[20] Yang M, Li J and Liu B 2018 *J. Alloys Compd.* **735** 1023
[21] Yang G, Xu B, Kong L, Li J and Zhao S 2016 *J. Alloys Compd.* **688** 88
[22] Peng C X, Sopu D, Cheng Y, Song K K, Wang S H, Eckert J and Wang L 2019 *Materials & Design* **168** 107662
[23] Feng S D, Li L, Chan K C, Qi L, Zhao L, Wang L M and Liu R P 2019 *J. Alloys Compd.* **770** 896
[24] Cao Q P, Li J F, Hu Y, Horsewell A, Jiang J Z and Zhou Y H 2007 *Materials Science and Engineering: A* **457** 94
[25] Sun P, Peng C, Cheng Y, Zhang G, Wang P, Jia L and Wang L 2019 *Computational Materials Science* **163** 290
[26] Zhao Y, Peng X, Yang B, Huang C, Hu N and Yan C 2019 *Ceramics International* **45** 19845

[27] Ning Z, Liang W, Kang Z, Sun H and Sun J 2017 *Materials Science and Engineering: A* **697** 233

[28] Zhou H, Qu S and Yang W 2013 *International Journal of Plasticity* **44** 147

[29] Wu Y, Wang H, Wu H H, Zhang Z Y, Hui X D, Chen G L, Ma D, Wang X L and Lu Z P 2011 *Acta Materialia* **59** 2928

[30] Song K K, Pauly S, Zhang Y, Li R, Gorantla S, Narayanan N, Kühn U, Gemming T and Eckert J 2012 *Acta Materialia* **60** 6000

[31] Wu Y, Xiao Y, Chen G, Liu C T and Lu Z 2010 *Adv. Mater.* **22** 2770

[32] Yue X X, Liu C T, Pan S Y, Inoue A, Liaw P K and Fan C 2018 *Physica B* **547** 48

[33] Li Y, Qiu S B, Shao Y and Yao K F 2011 *Chin. Phys. Lett.* **28** 116104

[34] Huang Y, Fan H, Wang D, Sun Y, Liu F, Shen J, Sun J and Mi J 2014 *Materials & Design* **58** 284

[35] Yang L, Guo G Q, Chen L Y, LaQua B and Jiang J Z 2014 *Intermetallics* **44** 94

[36] Singh D, Mandal R K, Tiwari R S and Srivastava O N 2015 *J. Alloys Compd.* **648** 456

[37] Feng S D, Chan K C, Chen S H, Zhao L and Liu R P 2017 *Scientific Reports* **7** 40969

[38] Pan J, Wang Y X, Guo Q, Zhang D, Greer A L and Li Y 2018 *Nat. Commun.* **9** 560

[39] Sheng H W, Luo W K, Alamgir F M, Bai J M and Ma E 2006 *Nature* **439** 419

[40] Cheng Y Q, Sheng H W and Ma E 2008 *Phys. Rev. B* **78** 014207

[41] Liu R, Wu J, Hai R, Zhong H, Li P, Xue P, Tan M J, Yang Y and Fu X 2024 *Journal of Materials Research and Technology* **32** 1342

[42] Zhang C, Liu H S and Peng H L 2023 *Chin. Phys. B* **32** 116101

[43] He Y, Ma C, Li S, Yi P, Liu H, Yang W, Chen Z, Zhang P, Chen C and Shen B 2024 *Materialia* **33** 102017

[44] Shao Y F, Meng F S, Li J H and Zhao X 2019 *Acta Phys. Sin.* **68** 216201 (in Chinese)

[45] Plimpton S 1995 *Journal of Computational Physics* **117** 1

[46] Mendelev M I, Sun Y, Zhang F, Wang C Z and Ho K M 2019 *The Journal of Chemical Physics* **151** 214502

[47] Wu J, Zhu M, Li S, Zhong H, Li P, Song K, Song W, Tan M J, Yang Y and Fu X 2024 *Materials Today Communications* **40** 109474

[48] Zhou Z, Zhu M, He Y, Wu J, Lin Y, Li P, Tan M J, Yang Y and Fu X 2023 *J. Alloys Compd.* **968** 172049

[49] Şopu D, Yuan X, Moitzi F, Stoica M and Eckert J 2019 *Materials* **12** 1419

[50] Fu X, Wu J, Zhou Z, Tan M J, Huang Y, Sun J, Song W, Guan P, Yang Y, Li Y and Ritchie R O 2025 *Acta Materialia* **287** 120787

[51] Fu X, Lin Y, Zhu M, Wang K, Wu J, Tong X, Song W, Tan M J, Yang Y, Shen J, Wang G, Shek C H and Ritchie R O 2023 *npj Computational Materials* **9** 226

[52] Shimizu F, Ogata S and Li J 2007 *Materials Transactions* **48** 2923

[53] Stukowski A 2010 *Modelling and Simulation in Materials Science and Engineering* **18** 015012

[54] Li M Z, Peng H L, Hu Y C, Li F X, Zhang H P and Wang W H 2017 *Chin. Phys. B* **26** 016104

[55] Pan J, Chen Q, Liu L and Li Y 2011 *Acta Materialia* **59** 5146

[56] Amigo N, Urbina F and Valencia F 2020 *Computational Materials Science* **184** 109941

[57] Liu Z Q, Liu G, Qu R T, Zhang Z F, Wu S J and Zhang T 2014 *Scientific Reports* **4** 4167

[58] Idury K S N S, Murty B S and Bhatt J 2016 *J. Non-Crystal. Solids* **454** 59

[59] Li M Z 2014 *Journal of Materials Science & Technology* **30** 551

[60] Feng S, Qi L, Wang L, Pan S, Ma M, Zhang X, Li G and Liu R 2015 *Acta Materialia* **95** 236